Simulation of the Sensing Performance of a Plasmonic Biosensor Based on Birefringent Solid-Core Microstructured Optical Fiber

Simulation of the Sensing Performance of a Plasmonic Biosensor Based on Birefringent Solid-Core Microstructured Optical Fiber

A finite element method is used to analyze the performance of a microstructured optical fiber based surface plasmon resonance sensors aimed for biomedical applications, such as the detection of blood carried species. Birefringence obtained by removing of a row of holes in a two-ring hexagonal lattice of holes in a gold covered silica fiber leads to relatively high sensitivity of the fiber optical response to a refractive index of the analyte surrounding the fiber. This fiber structure supports two types (I and II) of resonant modes. In these modes there is an opposite variation of some sensing parameters with the increase of the refractive index of the analyte between 1.36 and 1.39. Thus, for a smaller value (1.36) of the refractive index of the analyte n_a, the resonance spectral width $\delta\lambda_{0.5}$ is large for the core mode I and small for the core mode II but for a larger value (1.39) of n_a, $\delta\lambda_{0.5}$ is small for the core mode I and large for the core mode II. Also, for $n_a = 1.36$ the amplitude sensitivity S_A is small for the core mode I and large for the core mode II but for $n_a = 1.39$, S_A is large for the core mode I and small for the core mode II. By adjusting the radius of the gold layer, the proposed sensor shows high spectral sensitivity S_λ and narrow $\delta\lambda_{0.5}$ at the same resonance wavelength and n_a (1.39) where the figure of merit (*FOM*) is very large in comparison with the most recently published values.

Keywords: Sensors, surface plasmon resonance, finite element method

V. A. Popescu, N. N. Puscas
Department of Physics, University Politehnica of Bucharest,
Bucharest 060042 Romania
e-mail (corresponding author: V A Popescu): vapopescu@yahoo.com

G. Perrone
Department of Electronics and Telecommunications, Politecnico di Torino,
C.so Duca degli Abruzzi 24, I-10129 Torino

Introduction

Microstructured optical fiber-based plasmonic devices have attracted a large interest [1-8] for their application in chemical and biochemical sensing because of their large sensitivity combined with the possibility to easily tailor their properties by varying the geometry of the photonic crystal fiber. For instance, by changing the hole number and position the phase matching [1] or the loss matching [2-3] conditions between the fundamental HE_{11} core mode and a plasmon mode can be achieved.

In search of new approaches to enhance the sensitivity, recently, quite a number of papers have proposed new photonic crystal structures that exploit asymmetries to induce birefringence. An example is in [4], which uses a two ring hexagonal lattice photonic crystal fiber arrangement and the gold layer and the analyte are not placed inside the air-holes but outside the fiber structure, allowing a simplification in the fabrication process [2-3]. The obtained spectral sensitivity S_λ is 4000 nm/RIU (RIU stands for Refractive Index Units) when the refractive index of the analyte n_a is varied from 1.33 to 1.34 and 2000 nm/RIU when n_a is varied from 1.36 to 1.37; the amplitude sensitivity S_A is 320 RIU^{-1} for $n_a = 1.36$. In another recent paper [5], a D-shaped hollow core microstructured optical fiber-based surface plasmon resonance sensors is proposed: in this case S_λ and S_A values of 2900 nm/RIU and 120 RIU^{-1}, respectively, when n_a is varied from 1.33 to 1.34 have been reported. In another recent paper [6], an alternative plasmon D-shaped microstructured biosensor with rectangular lattice has been presented: the largest value of figure of merit (*FOM*) [13] is 478.3 RIU^{-1} and the lowest value of the resonance spectral width $\delta\lambda_{0.5}$ is 13.6 nm for the core guided mode; then for $n_a > 1.398$, a record value of $S_\lambda > 7481$ nm RIU^{-1} has been obtained, although multiple resonance peaks and large spectral width can deteriorate the signal-to-noise ratio.

In this paper a new microstructured birefringent fiber-based plasmonic sensor is introduced and its sensing characteristics are analyzed through a finite element method. The proposed structure is made of a two-ring hexagonal lattice with five of the central horizontal air holes suppressed and, as in [4], the gold layer and the analyte are outside the fiber structure [2], so to simplify its realization and use.

The Microstructured Plasmonic Optical Fiber Geometry

The considered microstructured optical fiber (Fig.1) is made by a SiO_2 core with fourteen small air holes placed at the vertices of a two-ring hexagonal lattice in which five central horizontal holes are omitted to introduce a birefringent behavior. The silica core is then further surrounded by gold and analyte layers. The structure is similar to that described in [4], except that in the proposed case the central hole and two air-holes in the same row - second ring are omitted. At the resonance wavelength, where there is a phase matching or a loss matching condition between a core mode and a plasmonic mode, this makes the *x*-component of the electric field in the sensing layer stronger than the corresponding *y*-component. In this fiber structure, there are two types of resonant modes: type I, when the main electric fields are oriented in the same x direction on the left and right sides of the gold layer; type II when orientations of these electric fields are in opposite directions. This allows maximizing the sensor performance by properly choosing the resonance mode type depending on the analyte expected refractive index value.

A finite element method is used to compute the propagation constants of the core and plasmon modes (mode index $\nu = 1$) in the structure and to analyze the power absorption

efficiency for these modes. The wavelength dependence of the refractive index of silica and gold, has been modeled by using, respectively, a Sellmeier formula for SiO_2 [9-11] and a Drude relation [12] for Au.

Numerical Results and Discussion

The proposed sensing structure is intended for biochemical applications, such as measurement of blood carried species for which the typical refractive index values of the analyte is in the range 1.36-1.39. Therefore, the radii and thickness parameters will be chosen to optimize the performance in this working range. For the same reason, the analysis has been carried out mainly for said refractive index values. In the first part of this section we report the results obtained from the analysis of the proposed microstructured optical fiber probe (Fig.1) in which the fourteen small air holes have all the same radius ($r = r_1 = r_2 = \ldots = r_{14} = 0.5$ μm) and are placed at the vertices of a two-ring hexagonal lattice with vertice-to-vertice distance $d = 2$ μm. As already pointed out, five central horizontal holes are then omitted to introduce the asymmetry that in turns induces the strong birefringent behavior. The SiO_2 substrate has radius $r_g = r_{15} = 5$ μm and is surrounded by a gold layer, with thickness $t_g = r_{16} - r_{15} = 40$ nm, followed by an analyte layer. These radii and thicknesses are the values giving the optimal sensor performance as it will be shown in the second part of this section, in which some results for slightly different values will be reported.

Table 1 shows the resonant wavelength λ, the effective indices β/k for the core and plasmon modes, the difference $\Delta(\beta/k)_r$ between the real parts of the effective indices of core and plasmon modes and the difference $\Delta(\beta/k)_i$ between the imaginary parts of the effective indices of the same modes. The values of the effective indices are given for the maximum value of the imaginary part of the core modes. Thus, when n_a is increased from 1.36 to 1.39 in the place of the phase matching point there is a loss matching point.

Fig.2 shows the contour plot of the z-component $S_z(x,y)$ of the Poynting vector at the phase matching point ($\lambda_{II} = 0.6575$ μm) between the core guided and the plasmon modes II for a photonic crystal fiber when the refractive index of the analyte is $n_a = 1.36$. Similarly, Fig.3 reports the contour plot of the z-component $S_z(x,y)$ of the Poynting vector at the loss matching point ($\lambda_I = 0.78135$ μm) between the core guided and the plasmon modes I for the same fiber structure when the refractive index of the analyte is $n_a = 1.39$. It is interesting to note that for $n_a = 1.39$, the value of the z-component $S_z(x,y)$ of the Poynting vector of the type I core guided mode at $x = 0$ is smaller than that obtained in the case of $n_a = 1.36$ (the power fraction transferred to the analyte layer is 0.022937 for $n_a = 1.36$ and 0.227788 for $n_a = 1.39$). At the resonance wavelength, the power fraction carried in the analyte layer increases with n_a for the core modes I and II (Table 2). Fig. 4 shows the real part of the effective index versus the wavelength for the core and plasmon modes near the loss matching point ($\lambda_I = 0.78135$ μm and $\lambda_{II} = 0.7990$ μm) when the refractive index of the analyte is $n_a = 1.39$. It is interesting to note that for each of the two types of modes I and II, there are anti-crossing points between plasmonic mode and core-guided mode and then the modes of each other exchange after the anticrossing point as in [6]. Fig. 5 shows the loss spectra for the core and plasmon modes near the loss matching point ($\lambda_I = 0.78135$ μm and $\lambda_{II} = 0.7990$ μm) for a photonic crystal fiber when the refractive index of the analyte is $n_a = 1.39$. Fig. 6 reports the imaginary part of the effective index versus the wavelength for the type I and II core modes near the resonance wavelength for two slightly different values of the analyte refractive index ($n_a = 1.39$ and $n_a = 1.391$). As expected, the core

guided mode and the plasmon mode are strongly coupled at the loss matching point in comparison with the case of phase matching point. This fact is responsible for the larger value of the power fraction carried in the analyte layer by the core mode (0.022937 for mode I and 0.152933 for mode II when n_a = 1.36 and 0.227788 for mode I and 0.273888 for mode II when n_a = 1.39). Also, in these modes there is an opposite variation of the resonance spectral width $\delta\lambda_{0.5}$ with the increase of the refractive index of the analyte. Thus, for a smaller value (1.36) of the refractive index of the analyte n_a, the resonance spectral width $\delta\lambda_{0.5}$ is large (30.9 nm) for the core mode I and small (14.6 nm) for the core mode II but for a larger value (1.39) of n_a, $\delta\lambda_{0.5}$ is small (12.2 nm) for the core mode I and large (54 nm) for the core mode II.

The maximum values of the amplitude sensitivity S_A and the corresponding resolutions (assuming that a 1 % change in the transmitted intensity can be detected) for the guided modes I and II are given in Table 2 for different values of the analyte refractive index, namely 1.36, 1.37, 1.38 and 1.39. Fig. 7 shows the amplitude sensitivity for the guided core modes (I and II) versus the wavelength near the resonance wavelength (λ_{I} = 0.6552 μm and λ_{II} = 0.6575 μm when n_a = 1.36 and λ_{I} = 0.78135 μm and λ_{II} = 0.7990 μm when n_a = 1.39). It is interesting to note that for n_a = 1.36 the amplitude sensitivity S_A is small (192.6 RIU^{-1}) for the first core mode I and large (405.7 RIU^{-1}) for the second core mode II but for n_a = 1.39, S_A is large (886.9 RIU^{-1}) for the first mode I and small (245.8 RIU^{-1}) for the second mode II. Fig. 8 shows the resonance spectral width $\delta\lambda_{0.5}$ and the amplitude sensitivity S_A for the core modes (I,II) with the increase of the refractive index of the analyte from n_a = 1.35 to n_a = 1.40. One observe that there is a dip of $\delta\lambda_{0.5}$ = 14.6 nm at n_a = 1.36 for the core mode II and another dip of $\delta\lambda_{0.5}$ = 12.2 nm at n_a = 1.39 for the core mode I. Also there is a peak of S_A = 405.7 RIU^{-1} at n_a = 1.36 for the core mode II and another peak of S_A = 886.9 RIU^{-1} at n_a = 1.39 for the core mode I.

Table 2 summarizes also all the relevant parameters of type I and II core modes to fully characterize the sensor performance: phase or the loss matching points, transmission loss α, propagation length L, power fraction P_1 in the analyte layer; power fraction P_2 in the gold layer; shift $\delta\lambda_{res}$ towards longer wavelengths of the phase matching point or loss matching point for an increase Δn_a of the analyte refractive index by 0.001 RIU; resonance spectral width $\delta\lambda_{0.5}$ (computed at the full width at half maximum of the loss spectra); signal-to-noise ratio *SNR*; spectral sensitivity S_λ; spectral resolution SR_λ (detection limit in the wavelength interrogation mode, assuming a spectral resolution of 0.1 nm); maximum value of the amplitude sensitivity S_A and the corresponding resolution; difference $\Delta\lambda$ between maximal amplitude sensitivity and resonant wavelengths; the figure of merit *FOM,* which is defined as the ratio between the spectral sensitivity S_λ and $\delta\lambda_{0.5}$ [13].

Besides the refractive index of the analyte layer, the resonance condition, sensor sensitivity and the loss or the phase matching condition are determined by the radii of the gold layer and of the small air holes, the thickness of the gold layer. Thus, for an increase of the radius r_g of the gold layer by 1 μm (that is for r = 0.5 μm, r_g = 6 μm, t_g = 40 nm and d = 2 μm), the phase matching point for the core modes I(II) shifts by 7.5 nm (0.3 nm) towards longer wavelengths when n_a = 1.36. Correspondingly, the shift $\delta\lambda_{res}$ is 3.1 nm (3.4 nm), whereas the spectral resolution SR_λ is 3.2×10^{-5} RIU (2.9×10^{-5} RIU).

For a decrease of the radius r_g of the gold layer by 0.45 μm (that is for r = 0.5 μm, r_g = 4.55 μm, t_g = 40 nm, d = 2 μm), the phase matching point for the core modes I(II) shifts by 4.2 nm (3.0 nm) towards shorter wavelengths when n_a = 1.36. Correspondingly, the shift $\delta\lambda_{res}$ is

2.5 nm (2.7 nm), whereas the spectral resolution SR_λ is 4.0×10^{-5} RIU (3.8×10^{-5} RIU). On the other hand for the same modified structure but when n_a =1.39, the parameters of the core modes I(II) become: $\delta\lambda_{res}$= 6.3 nm (7.4 nm), $\delta\lambda_{0.5}$= 11.8 nm (46.4 nm), *SNR* = 0.53 (0.16), *FOM* = 532.3 RIU^{-1} (159.5 RIU^{-1}), S_λ = 6254 $nmRIU^{-1}$ (7400 $nmRIU^{-1}$), SR_λ = 1.6×10^{-5} RIU (1.4×10^{-5} RIU), S_A = 943.3 RIU^{-1} (235.0 RIU^{-1}), SR_A = 1.1×10^{-5} RIU (4.3×10^{-5} RIU), α = 504.2 dB/cm (532.9 dB/cm), L = 86.1 μm (81.5 μm), P_1 = 0.242701 (0.284722), P_2 = 0.001977 (0.002058), λ = 0.768936 μm (0.7881 μm) and $\Delta\lambda$ = 6.3 nm (13.9 nm). In this case, the effective indices β/k for the core and plasmon modes I at the loss wavelength (λ_I = 0.768936 μm) are 1.448113 + 0.000784i and 1.447656 + 0.000784i, respectively. The effective indices β/k for the core and plasmon modes II at the loss wavelength (λ_{II} = 0.7881 μm) are 1.443474 + 0.000820i and 1.446467 + 0.000821i, respectively. Thus, $\delta\lambda_{0.5}$ is very small, *FOM* is high and S_A is very high for the core mode I.

For an increase of the radius r of the small air holes by 0.1 μm (that is for r = 0.6 μm, r_g = 5 μm, t_g = 40 nm and d = 2 μm), the phase matching point for the core modes I(II) shifts by 8.79 nm (11.1 nm) towards longer wavelengths when n_a = 1.39. Correspondingly, the shift $\delta\lambda_{res}$ is 7.5 nm (8.9 nm), whereas the spectral resolution SR_λ is 1.1×10^{-5} RIU (4.2×10^{-5} RIU). In this case, $\delta\lambda_{res}$ is very large (8.9 nm), $\delta\lambda_{0.5}$= 61.6 nm and the line shape of the wavelength-dependent loss is asymmetric for the core mode II.

For a decrease of the thickness of the gold layer by 10 nm (that is for r = 0.5 μm, r_g = 5 μm, t_g = 30 nm and d = 2 μm), the loss matching point for the core modes I(II) shifts by 58.2 nm (56.5 nm) towards shorter wavelengths when n_a = 1.39. Correspondingly, the shift $\delta\lambda_{res}$ is 5.9 nm (7.0 nm), whereas the spectral resolution SR_λ is 1.7×10^{-5} RIU (1.4×10^{-5} RIU). Also, the transmission loss for the guided modes I(II) is decreased to 280.1 dB/cm (294.3 dB/cm) and the power fraction carried in the analyte layer by the core mode is only 0.127993 for mode I and 0.150925 for mode II. In this case, the larger value of $\delta\lambda_{0.5}$ for higher n_a is due to a supplementary interaction between core mode II (mode index ν = 1) and a higher order plasmon mode (mode index ν = 2) at the wavelength 0.6928 μm with a large loss (312.4 dB/cm) and with a large power fraction (0.130845) in the analyte layer.

Conclusions

The proposed photonic fiber-based plasmonic sensor with a thin gold layer and fourteen small air holes supports two types of resonant modes with a strong interaction between the core and plasmon modes near the phase or the loss matching points. The two modes can be best exploited depending on the analyte refractive index value. Type II core guided mode resonances are most suited when $n_a \cong 1.36$; it exhibits higher loss (889.8 dB/cm), smaller propagation length (48.8 μm), smaller bandwidth value (14.6 nm) of bandwidth, large amplitude sensitivity (405.6 RIU^{-1}), very small difference between the wavelength for maximal amplitude sensitivity and the resonant wavelength (3.5 nm) and a symmetric line shape of the wavelength-dependent loss. On the other hand, for higher analyte refractive index values, say $n_a \cong 1.39$, type I core guided mode exhibits better results: higher spectral sensitivity (7000.0 $nmRIU^{-1}$), higher *SNR* ratio (0.57), very large *FOM* (573.8 RIU^{-1}) in comparison with the most recently published values [6], higher amplitude sensitivity (886.9 RIU^{-1}), better value of the detection limit of the amplitude-based sensor (1.1×10^{-5} RIU), smaller value (12.2 nm) of

bandwidth and the wavelength dependence of the imaginary part of the effective index is also symmetric. For $n_a \cong 1.38$ (refractive index for the whole human blood [14]) one can improve the information from our sensor by using both types of modes (Table 2). The basis structure that contains 14 holes where five central horizontal holes are omitted can be extended to a larger radius of the gold layer with a large number of rings in the lattice of the holes.

References

1. Skorobogatiy M, (2009) Microstructured and photonic bandgap fibers for applications in the resonant bio-and chemical sensors. J. Sens. 524237: 1-20, doi:10.1155/2009/524237
2. Popescu VA, Puscas NN and Perrone G (2012) Power absorption efficiency of a new microstructured plasmon optical fiber. J. Opt. Soc. Am. B 29(11): 3039-3046, doi:10.1364/JOSAB.29.003039
3. Popescu VA, Puscas NN and Perrone G (2014) Strong power absorption in a new microstructured holey fiber-based plasmonic sensor. J. Opt. Soc. Am. B 31(5): 1062-1070, doi:10.1364/JOSAB.31.001062
4. Rifat AA, Mahdiraji GA, Sua YM, Shee YG, Ahmed R, Chow DM, and Adikan FRM (2015) Surface plasmon resonance photonic crystal fiber biosensor: a practical sensing approach. IEEE Photonics Technology Letters 27(15): 1628-1631, doi:10.1109/LPT.2015.2432812
5. Luan N, Wang R, Lv W and Yao J (2015) Surface plasmon resonance sensor based on Dshaped microstructured optical fiber with hollow core. Opt Express 23(7):8576-8582, doi:10.1364/OE.23.008576
6. Peng L, Shi F, Zhou G, Hou Z and Xia C (2015) A surface plasmon biosensor based on a D-shaped microstructured optical fiber with rectangular lattice. IEEE Photon. J. 7(5): 1-9, doi:10.1109/JPHOT.2015.2488278
7. Shuai B, Xia L, Zhang Y, Liu D (2012) A multi-core holey fiber based plasmonic sensor with large detection range and high linearity. Opt Express 20(6):5974–5986, doi:10.1364/OE.20.005974
8. Zhang Y, Xia L, Zhou C, Yu X, Liu H, Liu D, and Zhang Y (2011) Microstructured fiber based plasmonic index sensor with optimized accuracy and calibration relation in large dynamic range. Opt. Commun. 284(18): 4161- 4166, doi:10.1016/j.optcom.2011.04.053
9. Sharma AK, Rajan R and Gupta BD (2007) Influence of dopants on the performance of a fiber optic surface plasmon resonance sensor. Opt. Commun. 274(2): 320-326
10. Verma RK, Sharma AK and Gupta BD (2008) Surface plasmon resonance based tapered fiber optic sensor with different taper profiles. Opt. Commun. 281**:** 1486-1491
11. Ghatak AK and Thyagarajan K (1999) Introduction to Fiber Optics (Cambridge University Press)
12. Vial A, Grimault AS, Macías D, Barchiesi D, and Chapelle ML (2005) Improved analytical fit of gold dispersion: Application to the modeling of extinction spectra with a finite-difference time-domain method. Phys. Rev. B 71: 085416, doi: 10.1103/PhysRevB.71.085416
13. Shalabney A and Abdulhalim I, (2012) Figure-of-merit enhancement of surface plasmon resonance sensors in the spectral interrogation. Opt Lett. 37(7):1175-1177, doi:10.1364/OL.37.001175
14. Sardar D and Levy L (1998) Optical properties of whole blood. Lasers Med. Sci. 13 (2):106–111, doi:10.1007/s101030050062

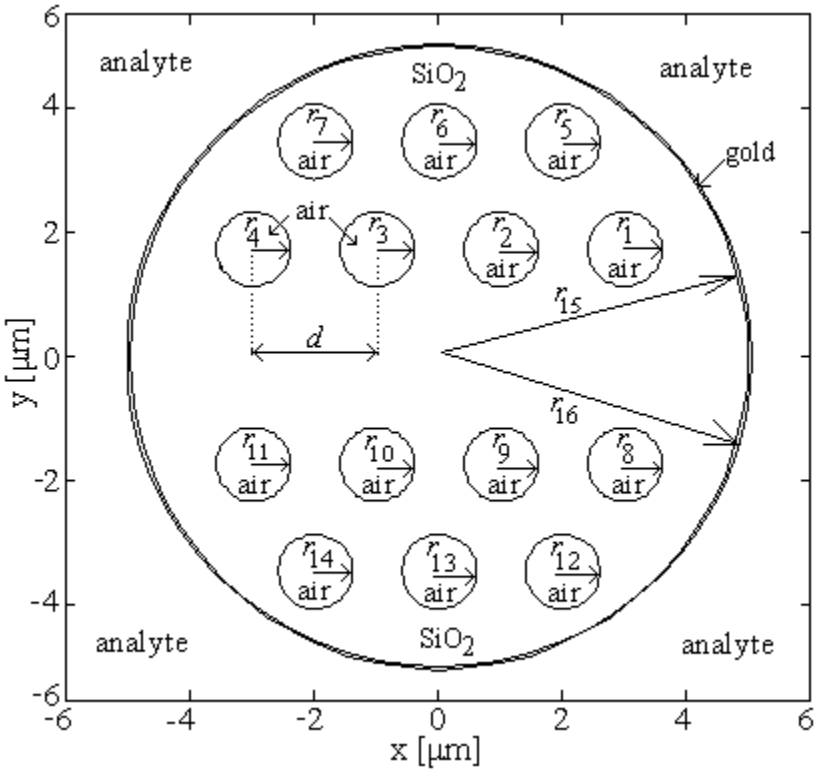

Fig.1**.** Cross section of a microstructured optical fiber made by fourteen small air holes (radius $r_1 = r_2 = \ldots = r_{14} = 0.5$ μm) which are placed at the vertices of a two-ring hexagonal lattice with vertice-to-vertice distance $d = 2$ μm (five central horizontal holes are omitted) that are inserted in a SiO_2 substrate (radius $r_{15} = 5$ μm) which is surrounded by a gold layer (thickness $r_{16} - r_{15} = 40$ nm) and by an analyte layer.

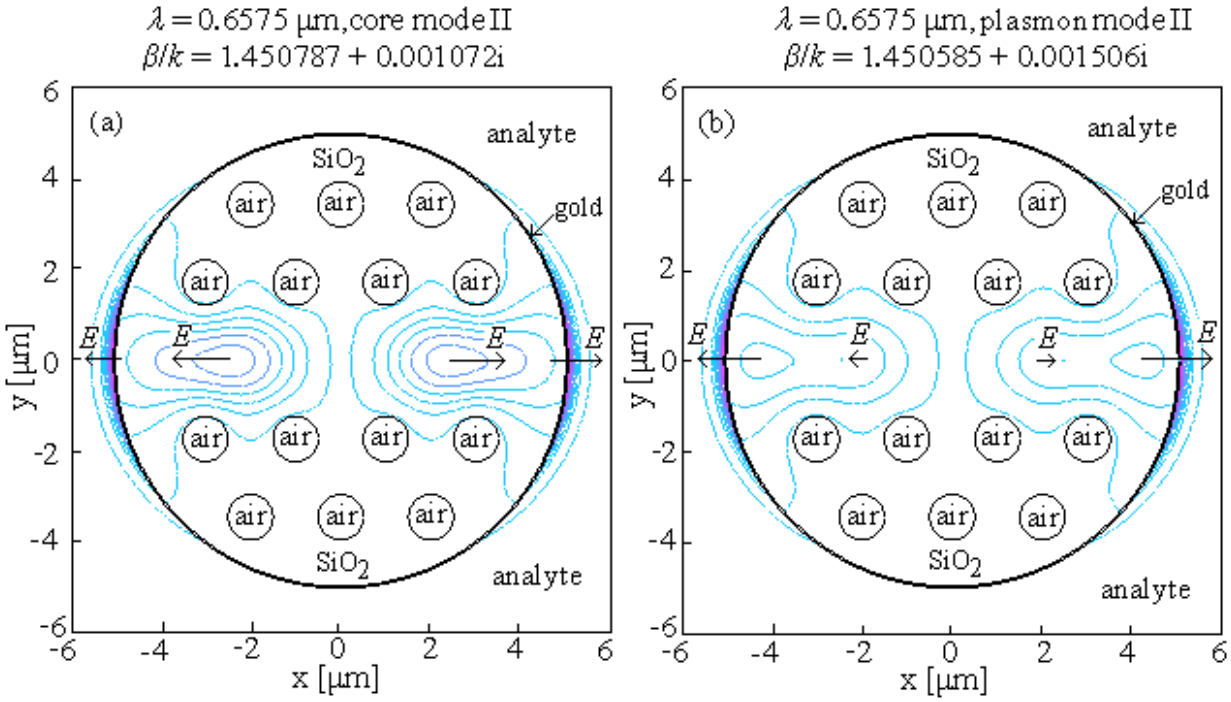

Fig.2. Contour plot of the z-component $S_z(x, y)$of the Poynting vector at the phase matching point (λ = 0.6575 μm) between the core guided (a) and the plasmon (b) modes (II) for a photonic crystal fiber (r_1 = r_2 = = r_{14} = 0.5 μm, r_{15} = 5 μm, r_{16} = 5.04 μm and d = 2 μm) when the refractive index of the analyte is n_a = 1.36. The main electric fields are oriented in the opposite x direction on the left and right sides of the gold layer.

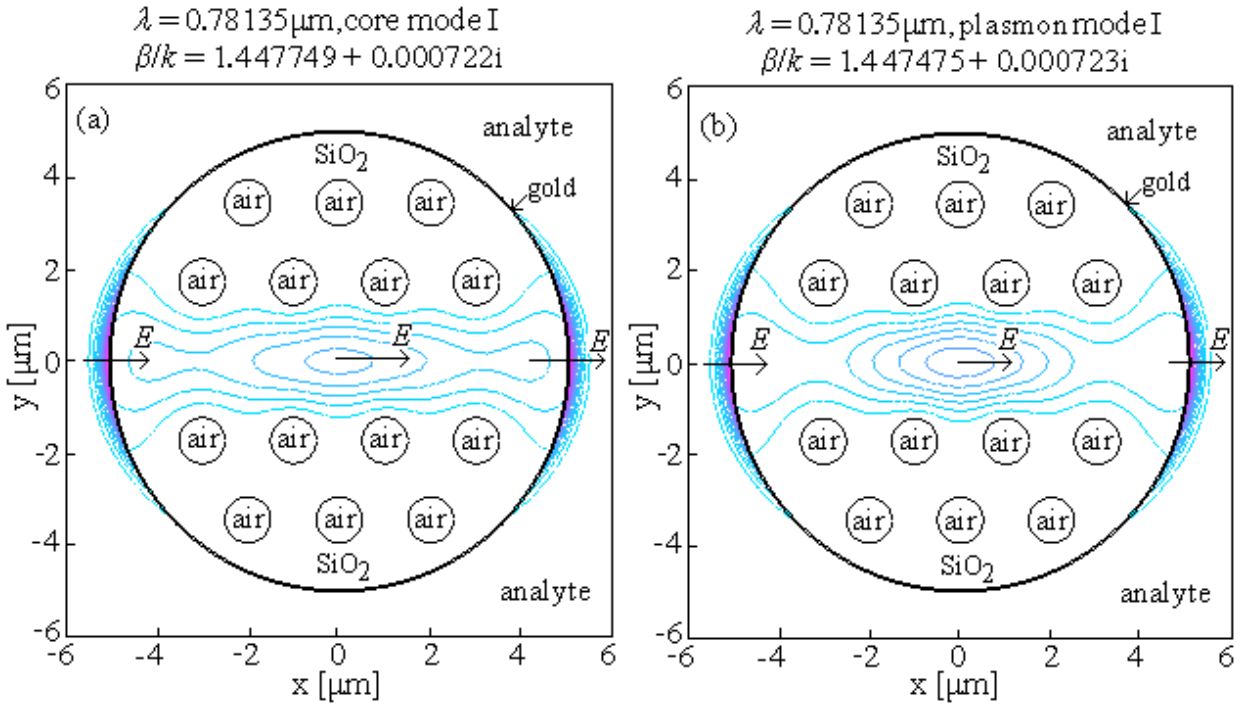

Fig.3. Contour plot of the z-component $S_z(x, y)$ of the Poynting vector at the loss matching point (λ = 0.78135 μm) between the core guided (a) and the plasmon (b) modes (I) for a photonic crystal fiber ($r_1 = r_2 = \ldots = r_{14}$ = 0.5 μm, r_{15} = 5 μm, r_{16} = 5.04 μm and d = 2 μm) when the refractive index of the analyte is n_a = 1.39. The main electric fields are oriented in the same x direction on the left and right sides of the gold layer.

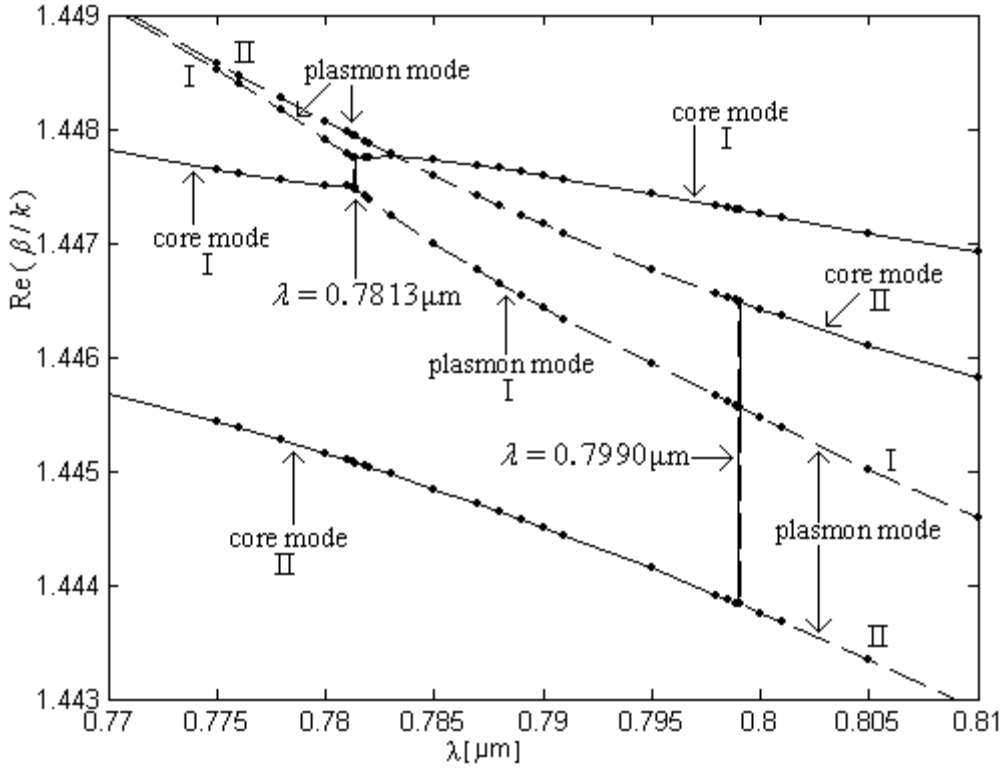

Fig. 4. The real part of the effective index versus the wavelength for the core and plasmon modes near the loss matching point (λ_{I} = 0.78135 μm and λ_{II} = 0.7990 μm) for a photonic crystal fiber ($r_1 = r_2 = \ = r_{14}$ = 0.5 μm, r_{15} = 5 μm, r_{16} = 5.04 μm and d = 2 μm) when the refractive index of the analyte is n_a = 1.39.

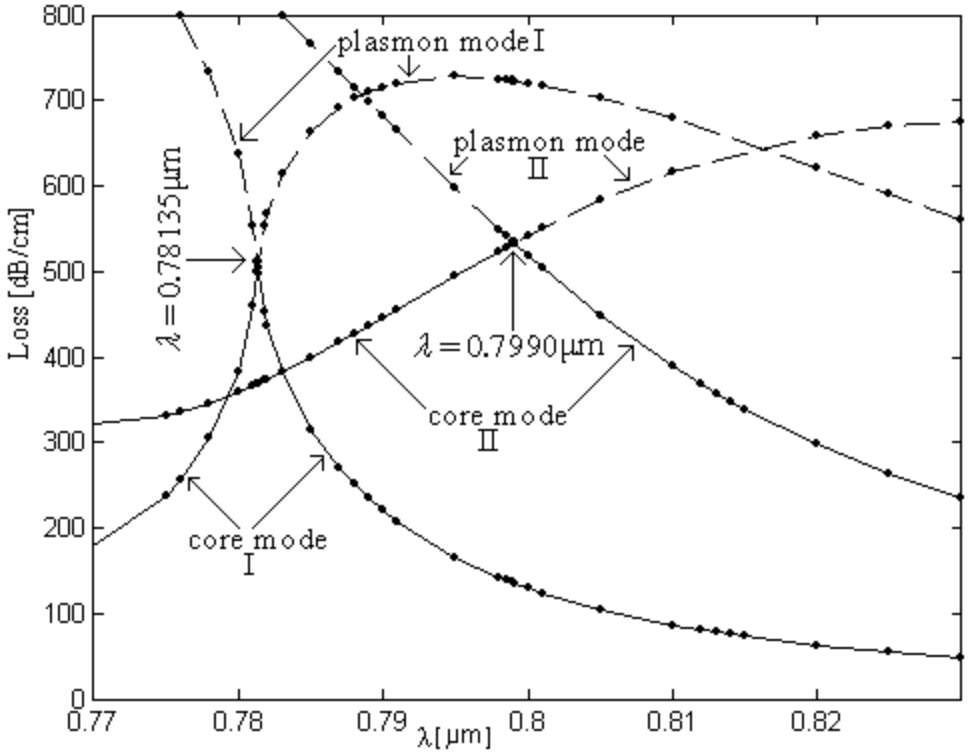

Fig. 5. The loss spectra for the core and plasmon modes near the loss matching point (λ_{I} = 0.78135 μm and λ_{II} = 0.7990 μm) for a photonic crystal fiber ($r_1 = r_2 = \ = r_{14}$ = 0.5 μm, r_{15} = 5 μm, r_{16} = 5.04 μm and d = 2 μm) when the refractive index of the analyte is n_a = 1.39.

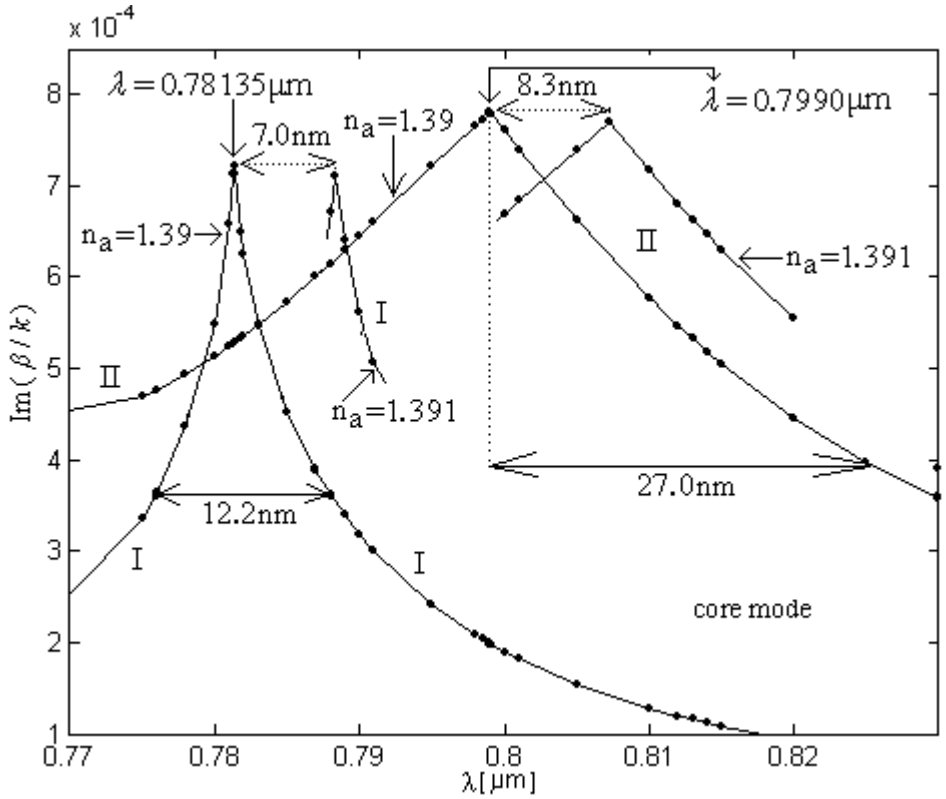

Fig. 6. The imaginary part of the effective index versus the wavelength for the core modes I and II near the resonance wavelength for a photonic crystal fiber ($r_1 = r_2 =$ $= r_{14} = 0.5$ μm, $r_{15} = 5$ μm, $r_{16} = 5.04$ μm and $d = 2$ μm) by varying the refractive index of the analyte from $n_a = 1.39$ to $n_a = 1.391$.

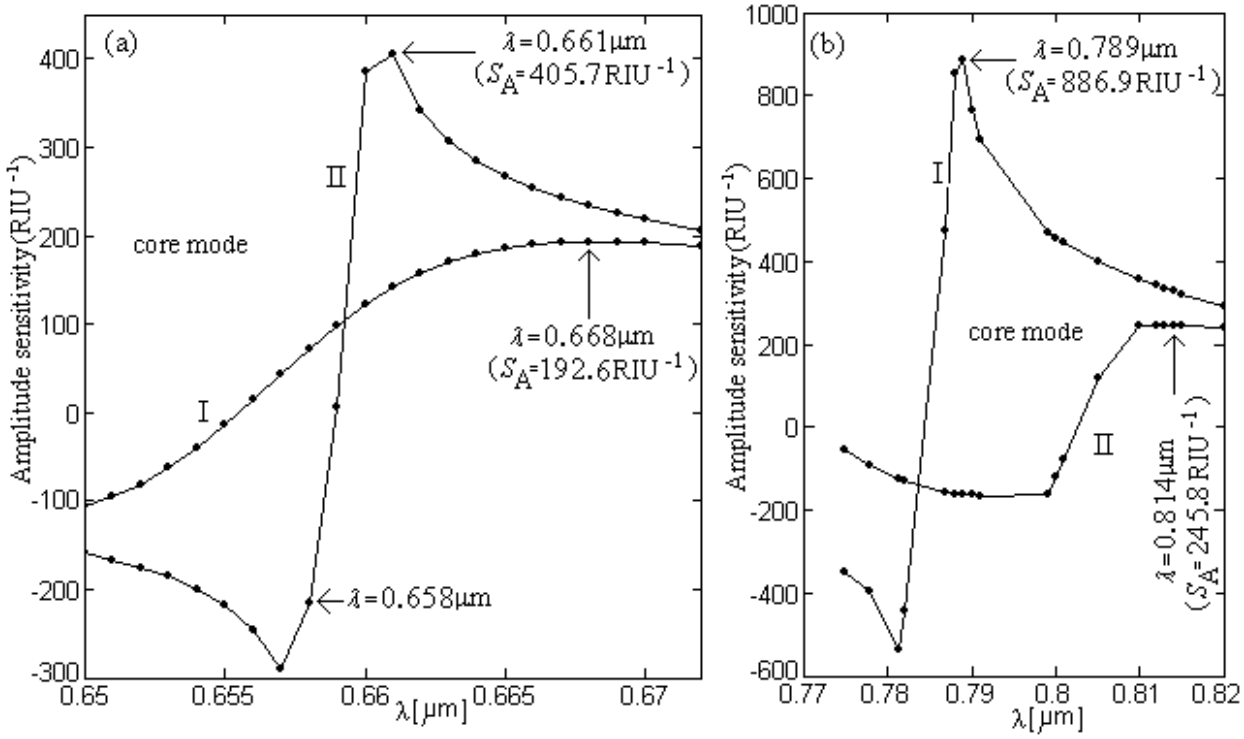

Fig. 7. The amplitude sensitivity for the guided modes (I and II) versus the wavelength near the resonance wavelength (λ_{I} = 0.6552 μm and λ_{II} = 0.6575 μm when n_a = 1.36 (a) and λ_{I} = 0.78135 μm and λ_{II} = 0.7990 μm when n_a = 1.39 (b)) for a photonic crystal fiber ($r_1 = r_2 = \ = r_{14}$ = 0.5 μm, r_{15} = 5 μm, r_{16} = 5.04 μm and d = 2 μm)

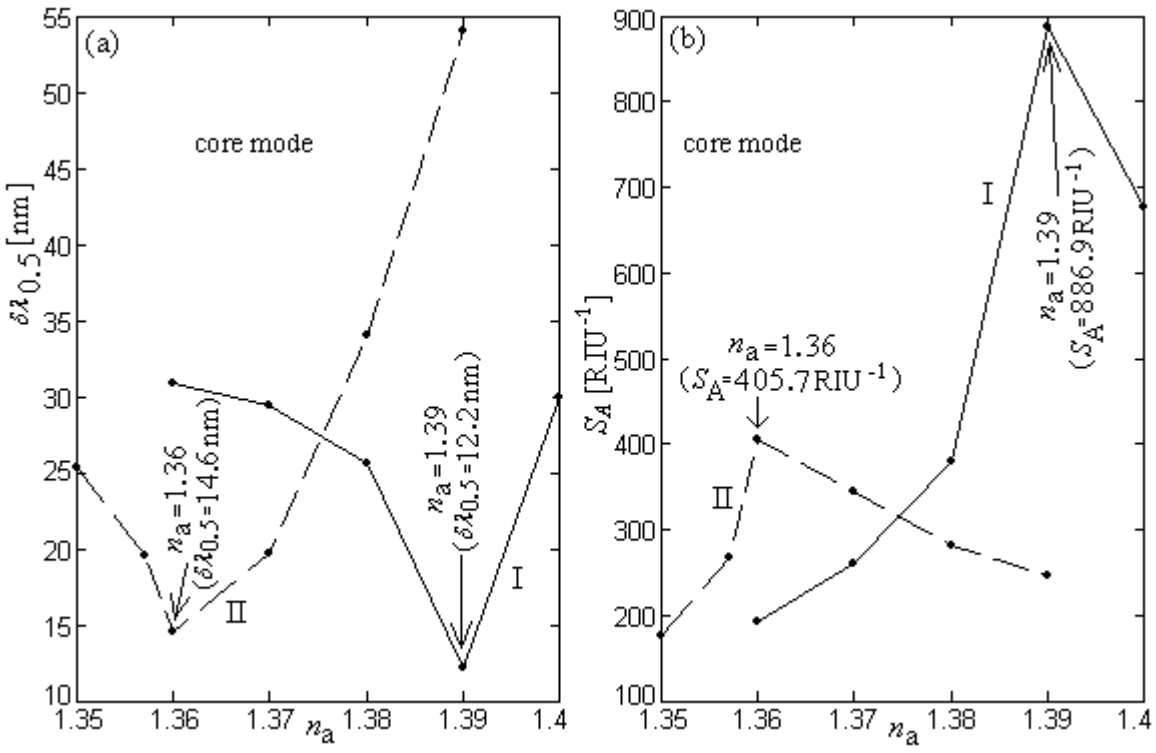

Fig. 8. The resonance spectral width $\delta\lambda_{0.5}$ (a) and the amplitude sensitivity S_A (b) for the core modes (I,II) with the increase of the refractive index of the analyte from n_a = 1.35 to n_a = 1.40.

Table 1. The resonant wavelength λ [μm], β/k for the core and plasmon modes, the difference $\Delta(\beta/k)_r$ between the real parts of the effective indices of core and plasmon modes and the difference $\Delta(\beta/k)_i$ between the imaginary parts of the effective indices of the same modes.

Mode (r_g;r; n_a)	λ [μm]	β/k (core) β/k (plasmon)	$\Delta(\beta/k)_r$	$\Delta(\beta/k)_i$
I (5;0.5;1.36)	0.6552	1.452097 + 0.000165i 1.451403 + 0.002141i	0.000694	0.001976
II (5;0.5;1.36)	0.6575	1.450787 + 0.001072i 1.450585 + 0.001506i	0.000202	0.000434
I (5;0.5;1.37)	0.6855	1.450949 + 0.000229i 1.450557 + 0.001726i	0.000392	0.001497
II (5;0.5;1.37)	0.69059	1.448537 + 0.001064i 1.450130 + 0.001064i	0.001593	0.000000
I (5;0.5;1.38)	0.7255	1.449520 + 0.000339i 1.449323 + 0.001334i	0.000197	0.000995
II (5;0.5;1.38)	0.7349	1.446499 + 0.000901i 1.448674 + 0.000903i	0.002175	0.000002
I (5;0.5;1.39)	0.78135	1.447749 + 0.000722i 1.447475 + 0.000723i	0.000274	0.000001
II (5;0.5;1.39)	0.7990	1.443833 + 0.000780i 1.446487 + 0.000782i	0.002654	0.000002

Table 2. Values of $\delta\lambda_{res}$[nm], $\delta\lambda_{0.5}$[nm], *SNR*, *FOM* [RIU^{-1}], S_λ[nmRIU^{-1}], SR_λ[RIU], S_A [RIU^{-1}], SR_A [RIU], α [dB/cm], L [μm], P_1, P_2, λ [μm] and $\Delta\lambda$ [nm] with increase of the refractive index of the analyte from $n_a = 1.36$ to $n_a = 1.39$.

Mode (r_g;r; n_a)	$\delta\lambda_{res}$ $\delta\lambda_{0.5}$	*SNR* *FOM*	S_λ SR_λ	S_A SR_A	α L	P_1 P_2	λ $\Delta\lambda$
I	2.7	0.09	2700	192.6	137.7	0.022937	0.6552
(5;0.5;1.36)	30.9	87.4	3.7×10^{-5}	5.2×10^{-5}	315.3	0.000460	12.8
II	2.7	0.18	2700	405.7	*889.8*	0.152933	0.6575
(5;0.5;1.36)	14.6	184.9	3.7×10^{-5}	2.5×10^{-5}	*48.8*	0.003003	*3.5*
I	3.5	0.12	3500	259.1	182.0	0.041625	0.6855
(5;0.5;1.37)	29.4	119.0	2.9×10^{-5}	3.9×10^{-5}	238.6	0.000635	11.5
II	3.9	0.20	3870	344.7	840.8	0.205089	0.69059
(5;0.5;1.37)	19.7	196.4	2.6×10^{-5}	2.9×10^{-5}	51.6	*0.003017*	4.6
I	4.7	0.18	4700	379.4	255.3	0.081271	0.7255
(5;0.5;1.38)	25.6	183.6	2.1×10^{-5}	2.6×10^{-5}	170.1	0.000898	9.5
II	5.3	0.16	5300	282.1	669.0	0.232833	0.7349
(5;0.5;1.38)	34.0	155.9	1.9×10^{-5}	3.5×10^{-5}	64.9	0.002420	7.1
I	7.0	*0.57*	7000	*886.9*	504.2	0.227788	0.78135
(5;0.5;1.39)	*12.2*	*573.8*	1.4×10^{-5}	*1.1×10^{-5}*	86.1	0.001685	7.7
II	*8.3*	0.15	*8250*	245.8	532.9	*0.273888*	0.7990
(5;0.5;1.39)	54.0*	152.8	*1.2×10^{-5}*	4.1×10^{-5}	81.5	0.001838	15.0

The optimized results are written with italicized characters. The symbol * refers to an assumed symmetric line shape of the wavelength-dependent loss.